Signature of Andreev-Bashkin superfluid drag from cavity optomechanics

Nalinikanta Pradhan [1], Rina Kanamoto [2], M. Bhattacharya [3] and Pankaj Kumar Mishra [1,*]

[1]Department of Physics, Indian Institute of Technology, Guwahati 781039, Assam, India

[2]Department of Physics, Meiji University, Kawasaki, Kanagawa 214-8571, Japan

[3]School of Physics and Astronomy, Rochester Institute of Technology, 84 Lomb Memorial Drive, Rochester, New York 14623, USA

(Received 30 October 2024; accepted 28 March 2025; published 14 April 2025)

The Andreev-Bashkin (AB) effect, corresponding to the dissipationless dragging of one superfluid by another, was predicted in the early 1970s but has so far eluded experimental detection. In this work, we theoretically introduce a detection paradigm and show that it enables the observation of the hitherto undetected AB effect for realistic parameters. We accomplish this by using the powerful techniques of cavity optomechanics, which were crucial to the observation of gravitational waves, on a spinor ring Bose-Einstein condensate. In contrast to established AB detection methods, our scheme allows for real-time, *in situ*, minimally destructive and three orders-of-magnitude-more-sensitive measurement of the AB effect. Our proposal, which considers persistent currents in weakly repulsive atomic condensates and amplifies the AB signal using a dynamic Bragg spectroscopy technique, is supported by numerical simulations of the stochastic Gross-Pitaevski equation, which agree very well with our analytic Bogoliubov–de Gennes calculations. Our work suggests a tool for sensitively and nondestructively probing the dynamics of rotationally interacting superfluids using cavities and has fundamental implications for ongoing studies of superfluid hydrodynamics, atomtronics, matter-wave interferometry, and cavity optomechanical sensing.

DOI: 10.1103/PhysRevResearch.7.023051

I. INTRODUCTION

The Andreev-Bashkin (AB) effect is a manifestation of macroscopic quantum coherence and describes nondissipative drag exerted by one superfluid on another. Originally considered for the ^{3}He-^{4}He system, where its observation is hindered by limited miscibility [1], ensuing predictions were made for superconductors [2], neutron stars [3], and polaritonic systems [4], but this fundamental effect has eluded observation since the early 1970s.

With the subsequent availability of highly pure and controllable cold atomic superfluids [5,6], there has been an intense revival of interest in observing the AB effect [7–9], with signatures expected from vortex formation [10,11], collective mode frequencies [12], spin-wave dynamics [8,13–16], transport in optical lattices [15,17–21] and droplets [22]. Special attention has been attached to geometries that are naturally suited for studies of atomic superflow, i.e., Bose-Einstein condensates (BECs) in ring traps [13,15,23,24]. In these systems, the challenges to be overcome for detection of the AB effect include monitoring of Josephson junctions [7], engineering and detection of soliton dynamics [25], operation in the strong-coupling regime of atomic interactions [13], species-selective addressal for rotation and observation, and maximization of the time-of-flight to improve signal contrast [26]. We note that all existing and proposed techniques are fully destructive of the superfluids, as they involve optical absorption imaging.

In this paper, we theoretically propose a real-time, *in situ*, minimally destructive and resolution-amplified detection of the AB effect, which is three orders of magnitude more sensitive than existing methods and proposals. As shown in Fig. 1, our proposal involves a spinor BEC [27] confined to a ring trap [28] inside a cavity driven by beams carrying optical orbital angular momentum (OAM) [29–31]. As demonstrated below, our method does not require Josephson junctions, soliton engineering, strong coupling, species-selective addressal, time-of-flight expansion or absorption imaging. Further, it gives direct access, via the optical cavity transmission, to the dynamics of OAM exchange—arising from the AB effect—between the two components of the superfluid BEC. Finally, it uses a dynamic Bragg spectroscopy technique to increase the resolution of the AB detection.

II. THEORETICAL MODEL

The central feature of the AB effect in a two-species mixture $[(\sigma, \sigma') \in 1, 2, \sigma \neq \sigma']$ is that the superfluid current J_σ of one component depends on the superfluid velocity $v_{\sigma'}$ of the other component [1,7,8]. In a two-component BEC, confined in a ring trap, this effect can be modeled by the one-dimensional quantum hydrodynamic

*Contact author: pankaj.mishra@iitg.ac.in

Hamiltonian [8,25,29,31]

$$\hat{H} = \sum_{\sigma} \int_{-\pi}^{\pi} \left\{ \Psi_{\sigma}^{\dagger}(\phi) \left[\frac{\hbar^2}{2mR^2} \left(-i\frac{d}{d\phi} - \frac{\Omega'}{2} \right)^2 \right] \Psi_{\sigma}(\phi) + \Psi_{\sigma}^{\dagger}(\phi)[\hbar U_0 \cos^2(\ell\phi) a^{\dagger} a] \Psi_{\sigma}(\phi) + \frac{g_{\sigma\sigma}}{2} \Psi_{\sigma}^{\dagger}(\phi) \Psi_{\sigma}^{\dagger}(\phi) \Psi_{\sigma}(\phi) \Psi_{\sigma}(\phi) + \frac{g_{\sigma\sigma'}}{2} \Psi_{\sigma}^{\dagger}(\phi) \Psi_{\sigma'}^{\dagger}(\phi) \Psi_{\sigma'}(\phi) \Psi_{\sigma}(\phi) + g_{d_{\sigma\sigma}} m J_{\sigma}^2/2 + g_{d_{\sigma\sigma'}} m J_{\sigma} J_{\sigma'} \right\} d\phi - \Delta_0 a^{\dagger} a - i\eta(a - a^{\dagger}), \quad (1)$$

where $\Psi_{\sigma,\sigma'}$ are the bosonic atomic field operators that obey the commutation relation $[\Psi_{\chi}(\phi), \Psi_{\chi}(\phi')] = \delta(\phi - \phi')$, where $\chi \in \sigma, \sigma'$. The first term in Eq. (1) represents the rotational kinetic energy in the frame corotating with the optical lattice, with frequency $\Omega = (\hbar/2mR^2)\,\Omega'$, where m is the atomic mass and R is the radius of ring trap (which can be set up, for example, using an optical field resonant with the cavity but very far detuned from the atomic transitions so that the field fluctuations have a negligible effect on the system dynamics [28]). The second term denotes the angular optical lattice potential created on the ring by the superposition of two Laguerre-Gaussian (LG) beams having topological charge $\pm\ell$, respectively [29,32], orthogonally polarized to and at a different wavelength than the ring trap field. For greater flexibility, it may be noted that the trap field can also be set up using a light wavelength at which the cavity mirrors are. transparent [33], thus allowing for independent detuning from atomic transitions as well as independent beam waist selection for good mode overlap between the trapping and lattice fields. Here $U_0 = g_0^2/\Delta_a$, where g_0 is the single photon-single atom coupling strength and Δ_a is the detuning of the optical lattice from the atomic transition. The photonic creation ($a^{\dagger}$) and annihilation (a) operators obey $[a, a^{\dagger}] = 1$.

The third and fourth terms in Eq. (1) represent the intraspecies and interspecies density-dependent atomic interactions, with the strengths $g_{\sigma\sigma}$ and $g_{\sigma\sigma'}$, respectively. The one-dimensional reduced atomic interaction is $g_{\sigma\chi} = 2\hbar\omega_{\rho} a_{s_{\sigma\chi}}/R$, where ω_{ρ} is the radial harmonic trap frequency and $a_{s_{\sigma\chi}}$ is the s-wave atomic scattering length between species σ and χ. The fourth-row terms denote the intraspecies and interspecies current-dependent atomic interactions with strength $g_{d_{\sigma\chi}}$ [25]. The probability current density of each component is $J_{\chi} = (\Psi_{\chi}^{*} \partial_{\phi} \Psi_{\chi} - \Psi_{\chi} \partial_{\Phi} \Psi_{\chi}^{*})\,\hbar/(2mRi)$. The first term in the last row represents the cavity field energy in the rotating laser drive frame, with Δ_0 being the de-tuning of the driving laser field frequency ω_L from the cavity resonance frequency ω_c. The last term denotes the coupling of the pump, at the rate $\eta = \sqrt{P_{\rm in}\gamma_0/(\hbar\omega_c)}$, where $P_{\rm in}$ is the input optical power and γ_0 is the cavity energy decay rate.

By scaling the energy as $\hbar\omega_{\beta} = \hbar^2/2mR^2$ and time as $\tau = \omega_{\beta} t$, from the Hamiltonian [Eq. (1)], and using quantum noise theory [29], the coupled dimensionless stochastic quantum hydrodynamic equations for the condensate order parameters ψ_{σ} (classical wave functions equivalent to the atomic operators Ψ_{σ} [5]) and the light field amplitude α can be written as [25,30,31]

$$(i - \Gamma)\frac{d\psi_{\sigma}}{d\tau} = -\frac{d^2\psi_{\sigma}}{d\phi^2} + \frac{U_0}{\omega_{\beta}} |\alpha|^2 \cos^2(\ell\phi)\,\psi_{\sigma} - \mu_{\sigma}\,\psi_{\sigma} - \Omega'\left(-i\frac{d}{d\phi}\right)\psi_{\sigma} + (\mathcal{G}_{\sigma\sigma}|\psi_{\sigma}|^2 + \mathcal{G}_{\sigma\sigma'}|\psi_{\sigma'}|^2)\,\psi_{\sigma} + \mathcal{G}_d\,(\mathcal{J}'_{\sigma\sigma} + \mathcal{J}'_{\sigma\sigma'}) + \xi(\phi, \tau), \quad (2)$$

and

$$i\frac{d\alpha}{d\tau} = \left\{ -\left[\Delta_0 - U_0 \langle \cos^2(\ell\phi) \rangle_{\tau} + i\frac{\gamma_0}{2} \right] \alpha + i\eta \right\} \omega_{\beta}^{-1} + i\sqrt{\gamma_0}\,\omega_{\beta}^{-1}\,\alpha_{\rm in}(\tau). \quad (3)$$

Here each condensate wave function ψ_{σ} is normalized to the number of atoms (N) as $\int_{-\pi}^{\pi} |\psi_{\sigma}(\phi, \tau)|^2\, d\phi = N$.

The first term on the right-hand side of the first row of Eq. (2) represents the scaled kinetic energy, the second term is the light-matter interaction [where $U_0 \cos^2(\ell\phi)/\omega_{\beta}$ is the effective optomechanical coupling between the light and each OAM plane-wave mode], and the last term denotes the scaled chemical potential, which serves to conserve the norm by being corrected at each time step as [34] $\Delta\mu_{\sigma} = (\Delta\tau)^{-1} \ln[\int |\psi_{\sigma}(\phi, \tau)|^2 d\phi / \int |\psi_{\sigma}(\phi, \tau + \Delta\tau)|^2 d\phi]$. The second term of the second row denotes the scaled intraspecies and interspecies density-dependent atomic interactions with strengths $\mathcal{G}_{\sigma\sigma} = g_{\sigma\sigma}/(\hbar\omega_{\beta})$ and $\mathcal{G}_{\sigma\sigma'} = g_{\sigma\sigma'}/(\hbar\omega_{\beta})$, respectively, and we use $\mathcal{G}' = \mathcal{G}_{\sigma\sigma'}/\mathcal{G}_{\sigma\sigma}$. In the third row, $\mathcal{J}'_{\sigma\sigma}$ and $\mathcal{J}'_{\sigma\sigma'}$ represent the scaled intraspecies and interspecies current-current interaction terms. Here $\mathcal{J}'_{\sigma\chi} = [2(\partial_{\phi}\psi_{\sigma})J'_{\chi} + \psi_{\sigma}(\partial_{\phi}J'_{\chi})]/2i$ and J'_{χ} is the scaled probability current density, expressed as $J'_{\chi} = (\psi_{\chi}^{*}\partial_{\phi}\psi_{\chi} - \psi_{\chi}\partial_{\Phi}\psi_{\chi}^{*})/(2i)$. The strength of these interactions is given by $\mathcal{G}_d = \mathcal{G}'_d/\rho_{\sigma}$, where $\rho_{\sigma} = N/2\pi$ is the condensate density. By comparing the drag energy density in Eq. (1) with the free energy density of a mixture of two superfluids, we obtain the drag parameter $\mathcal{G}'_d = 2g_{d_{\sigma\chi}}\rho_1 = 2\rho_d/\rho_1$, where $\rho_1 = \rho_2$ is the density of each component and ρ_d is the drag density arising due to the current coupling between two components [13]. The parameter $\mathcal{G}'_d$ depends on the interspecies and intraspecies density-density interactions [13], with more details on the appropriate range of values of $\mathcal{G}'_d$ given in the Appendix.

The classical mean-field dynamics of the intracavity light field amplitude α is governed by Eq. (3). Here we have treated the intracavity amplitude classically and neglected the effect of photon-number quantum fluctuations. This approximation is justified in the regime where the time period of mechanical oscillation is larger than the lifetime of cavity photons, $\omega_{1\pm,2\pm} \ll \gamma_0$ (Appendix B), i.e., the bad-cavity limit [35]. In this limit, which our parameters satisfy, the mechanical modes effectively interact with a large number ($\sim 10^3$) of photons per oscillation period, and therefore the light can be treated classically and its quantum fluctuations can be ignored. The second term within the square bracket of the right-hand side of Eq. (3) represents the coupling between the light mode and condensates, where the expectation value of the optical lattice potential is given by

$\langle \cos^2(\ell\phi)\rangle_\tau = \sum_\sigma \int_{-\pi}^{\pi} |\psi_\sigma(\phi,\tau)|^2 \cos^2(\ell\phi) d\phi$ [30,31]. The last terms of Eqs. (2) and (3) represent the thermal fluctuations $\xi(\phi,\tau)$ present in the condensate and the shot noise $\alpha_{\rm in}(\tau)$ carried by the laser light, respectively. Both are delta-correlated white noises having zero mean and unit variance with the correlations [31,36]

$$\langle \xi(\phi,\tau)\,\xi^*(\phi',\tau')\rangle = \frac{2\,\Gamma\,k_B\,T}{\hbar\omega_\beta}\,\delta(\phi-\phi')\,\delta(\tau-\tau'), \quad (4)$$

$$\langle \alpha_{\rm in}(\tau)\,\alpha^*_{\rm in}(\tau')\rangle = \omega_\beta\,\delta(\tau-\tau'), \quad (5)$$

where Γ and T denote the dissipation and temperature of the condensate, respectively, and k_B is the Boltzmann constant.

We solve Eqs. (2) and (3) in real time using a fourth-order Runge-Kutta scheme [37]. In our simulations, we consider ^{23}Na atoms in the two Zeeman states $|F, M_F\rangle = |1, \pm 1\rangle$, where $F(M_F)$ is the quantum number of atomic hyperfine (magnetic) angular momentum quantum number; the two states are rendered nondegenerate by a small uniform magnetic field [27]. The OAM-carrying beams are detuned to the ^{23}Na D_2 transition at 589 nm. We rotate the optical lattice at frequency Ω (this may be accomplished experimentally using spatial light modulators) such that $\cos^2(l\phi) \to \cos^2[l(\phi + \Omega'\tau)]$ in Eqs. (2) and (3), where $\Omega' = \Omega/\omega_\beta$ [30]. The parameter values used are $m = 23$ amu, $R = 12$ μm, $\Gamma = 0.0001$, $T = 10$ nK, $U_0 = 2\pi \times 212$ Hz, $\tilde{\Delta} = \Delta_0 - U_0 N = -2\pi \times 173$ Hz, $\Delta_a = 2\pi \times 4.7$ GHz, $\omega_c = 2\pi \times 10^{15}$ Hz, $\omega_\rho = \omega_z = 2\pi \times 42$ Hz, $\gamma_0 = 2\pi \times 2$ MHz, and $\Omega' = -1$ [38,39]. For the initial calculations, we have used the intraspecies scattering length $a_{s_{\sigma\sigma}} = 2.5$ nm and the interspecies scattering length $a_{s_{\sigma\sigma'}} = \mathcal{G}' a_{s_{\sigma\sigma}}$. Later in the paper, we address variations in the interaction strengths, considering that the various relevant ^{23}Na ground-state Zeeman states display nearly the same scattering lengths [40].

III. RESULTS

The initial wave functions assumed by us are

$$\psi_\sigma(\phi,0) = \sqrt{\frac{N}{2\pi}}\,e^{iL_{p_\sigma}\phi}, \quad (6)$$

where $\sigma \in 1, 2$, and L_{p_1} and L_{p_2} are the winding numbers of the two components, respectively. We consider one component initially rotating ($L_{p_1} \neq 0$) in the presence of a second, initially nonrotating $L_{p_2} = 0$ condensate. We have numerically verified that such supercurrent distributions are experimentally feasible via a rapid temperature quench [36,41] or by merging independent condensates in a ring trap [42]; an example is provided in Appendix. The AB drag effect facilitates the transfer of angular momentum from the initially rotating to the nonrotating component [1,25].

With these initial conditions, we simulate the system up to $t = 4$ s, well within the demonstrated lifetime of supercurrents, which is of the order of minutes [28,43]. The results of these simulations are shown in Figs. 2–4. The condensate density (blue) and phase (green) profiles of ψ_1 and ψ_2 are shown in Figs. 2(a) and 2(c). The phase profile of ψ_1 validates the winding number $L_{p_1} = 3$, while the phase profile of ψ_2, which was initially nonrotating, shows a blunted jump, indicating the presence of induced rotation in the second component. The high-frequency modulations in the condensate densities and phases arise due to the presence of the weak optical lattice trap in the ring BEC.

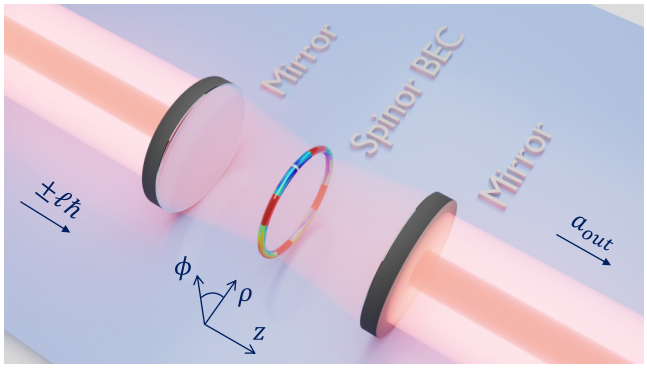

FIG. 1. Proposed experimental setup. A spinor BEC is confined in a ring trap inside an optical cavity. The cavity is driven by OAM-carrying optical beams which form an angular lattice on the ring.

To assess the rotational states of the two condensates, we show the matter-wave OAM distributions ($|\tilde{\psi}_\sigma(l)|^2$) in Figs. 2(b) and 2(d). These plane-wave modes constitute the mechanical degrees of freedom in our cavity optomechanical system. Here $\tilde{\psi}(l)$ is the Fourier transformation, taken in the frame of the rotating lattice for convenience, of the condensate wave function $\psi(\phi)$ into the matter-wave OAM basis. Due to Bragg scattering of the atoms from the optical lattice, a fraction of atoms undergo a change in their winding number from L_{p_σ} to $L_{p_\sigma} \pm 2\ell$ (since the photon number inside the cavity is less than one on average, the lattice is weak and higher-order diffraction is negligible [29,44]). The significant occupancies of the modes adjacent to L_{p_σ} and $L_{p_\sigma} \pm 2\ell$ in Figs. 2(b) and 2(d) indicate that the plane-wave states are

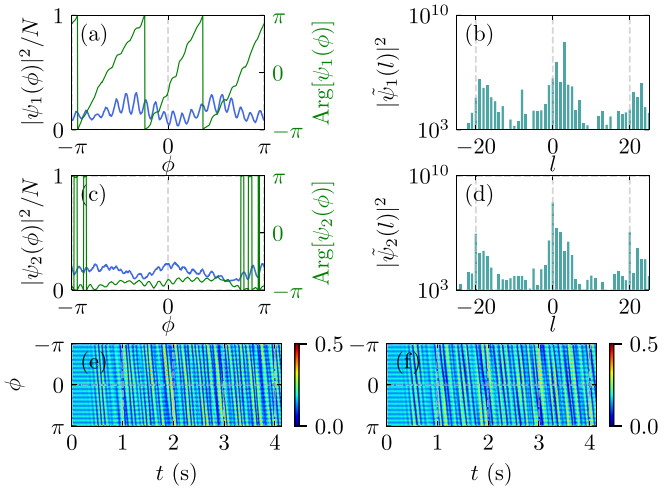

FIG. 2. [(a) and (c)] Condensate density (blue), phase (green) profiles, and [(b) and (d)] matter-wave OAM distributions of the two components ψ_1 and ψ_2 for $L_{p_1} = 3, L_{p_2} = 0$ after 4 s of time evolution. The other parameters are $\ell = 10$, $N = 1500$, $\Omega' = -1$, $\mathcal{G}' = 0.8$, $\mathcal{G}'_d = 0.095$, and $P_{\rm in} = 0.4$ pW. [(e) and (f)] Pseudocolor plots showing the temporal evolution of the condensate density profiles of ψ_1 and ψ_2, scaled by N.

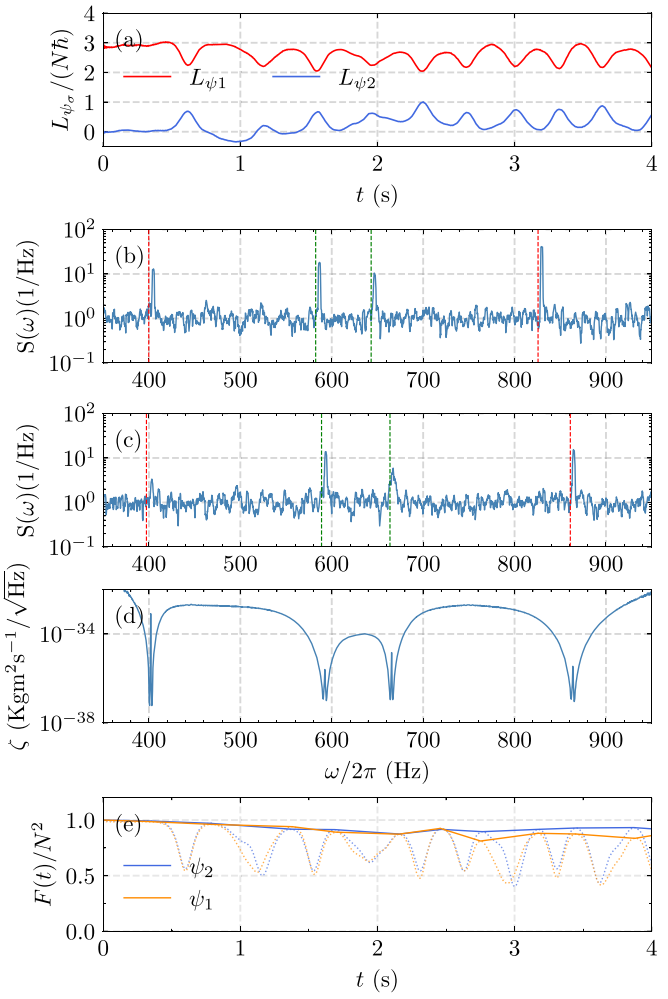

FIG. 3. (a) Temporal evolution of the angular momenta per atom of the two components. (b) Power spectra of the output phase quadrature of the cavity field in the absence of current-current coupling ($\mathcal{G}'_d = 0$, $\mathcal{G}' = 0.8$) and (c) in the presence of current-current coupling ($\mathcal{G}'_d = 0.095$, $\mathcal{G}' = 0.8$). The red (green) vertical dashed lines in (a) and (b) denote the analytical predictions for the side mode frequencies corresponding to $L_{p_1} \pm 2\ell - \Omega'/2$ ($L_{p_2} \pm 2\ell - \Omega'/2$) obtained from the BdG analysis. (d) Rotation measurement sensitivity versus system response frequency. Here $\Omega' = -1$, $G = 2\pi \times 2.90$ kHz, $|\alpha_s|^2 = 0.19$, and $t_{\text{meas}} = 24.6$ ms. (e) Variation of fidelity with time. The other parameters used are the same as in Fig. 2.

modulated to a solitonic state due to the transfer of angular momentum from rotating to nonrotating atoms [25]. (Few-mode plane-wave versus multimode solitonic matter-wave OAM distributions can be seen in our earlier work [31]). The real-time evolution of the density profiles, as illustrated in Figs. 2(e) and 2(f), reveals the occurrence of the density oscillations. This features suggests the dynamical formation of matter-wave solitons driven by the superfluid drag effect, which, in turn influences its subsequent motion in the ring trap, similarly to the observations made in Ref. [25].

We compute the angular momentum per atom of both superfluid components to demonstrate the drag. Particularly, Fig. 3(a) shows a repeated exchange of angular momentum between the components with time [25]. In our proposal, this

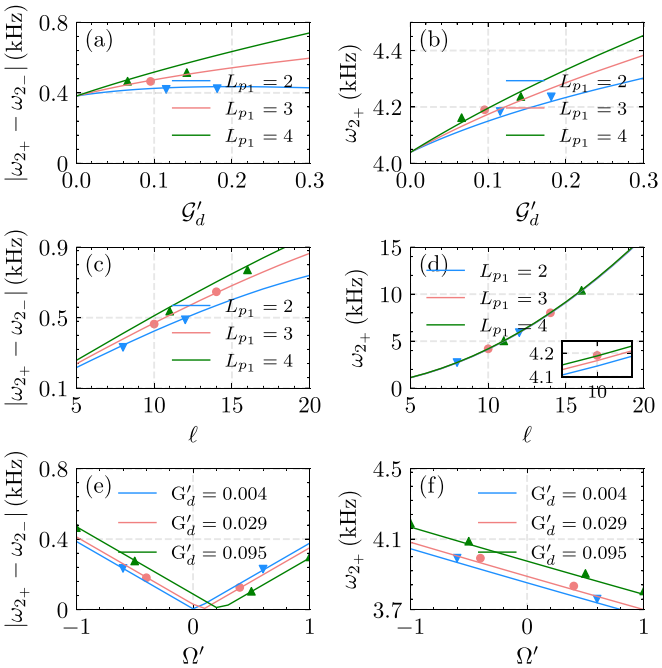

FIG. 4. Variation of the peak splitting $|\omega_{2_+} - \omega_{2_-}|$ and the peak location of ω_{2+} [(a) and (b)] with $\mathcal{G}'_d$ for $\ell = 10$, $\Omega' = -1$, [(c) and (d)] with ℓ for $\mathcal{G}'_d = 0.095$ ($\mathcal{G}' = 0.8$), $\Omega' = -1$, and [(e) and (f)] with Ω' for $L_{p_1} = 3$ and $\ell = 10$. The other parameters used are the same as in Fig. 2. The data points denoted by markers are obtained from the numerical simulations, whereas the lines are obtained from the Bogoliubov analysis.

exchange can be optically detected via homodyne measurement of cavity transmission [29,31]. The relevant theoretical quantity is the power spectrum of the phase quadrature of the cavity output field, defined as

$$S(\omega) = |\text{Im}[\alpha_{\text{out}}(\omega)]|^2, \tag{7}$$

where the cavity output field $\alpha_{\text{out}} = -\alpha_{\text{in}} + \sqrt{\gamma_0}\alpha$ is related to the input (α_{in}) and intracavity (α) fields [35]. Spectra, shown in Figs. 3(b) and 3(c) have well-resolved peaks at $\omega_{1\pm}$ (outer peaks) and $\omega_{2\pm}$ (inner peaks), corresponding to the matter-wave sidemodes with winding numbers $L_{p_1} \pm 2\ell - \Omega'/2$ and $L_{p_2} \pm 2\ell - \Omega'/2$, respectively, where $I = mR^2$ is the moment of inertia of each atom about the cavity axis. Identification of individual peaks is made possible by performing a Bogoliubov analysis (see details in the Appendix), and the frequencies obtained are indicated by vertical dashed lines in all cavity output spectra in Fig. 3.

We now examine how the cavity output spectra behave as the interactions in the system vary, an analysis crucial for identifying the AB effect. In the absence of *all* interspecies interactions (density-density as well as current-current) and no lattice rotation ($\Omega' = 0$), the initially nonrotating second component remains nonrotating ($L_{p_2} = 0$), and the $\omega_{2\pm}$ Bragg peaks are degenerate. Introducing *only* the density-density intercomponent interactions facilitates angular momentum transfer via counter superflow instability, as explained in Refs. [45,46] and the Appendix. It leads to splitting of the $\omega_{2\pm}$ peaks, which, however, can only be resolved by rotating the lattice ($\Omega' \neq 0$) as shown in Fig. 3(b). Finally, by

including the current-current interactions, which introduce the AB effect [8,25], further splitting of the $\omega_{2\pm}$ peaks is observed as can be seen in Fig. 3(c). This additional splitting is a clear signature of the AB effect and is the central result of this paper.

The effectiveness of our proposed method can be estimated by calculating its sensitivity to rotation measurements, which is defined as [29]

$$\zeta = \frac{S(\omega)}{\partial S(\omega)/\partial \Lambda} \times \sqrt{t_{\rm meas}}, \tag{8}$$

where $\Lambda = \hbar L_{p_2}$ is the angular momentum of the initially nonrotating condensate. Here $t_{\rm meas}^{-1} = 8(\alpha_s G)^2/\gamma_0$ is the optomechanical measurement rate in the bad-cavity limit, α_s is the steady state of the cavity field, and $G = U_0\sqrt{N}/2\sqrt{2}$ [29,35]. The sensitivity of rotation measurement on the initially nonrotating component is shown as a function of the system response frequency in Fig. 3(d). The best sensitivities of ($\sim 10^{-37}$ kg m^2 s$^{-1}/\sqrt{\rm Hz}$), obtained near the side-mode frequencies of the condensate, are about three orders of magnitude better than existing methods and schemes, which are all based on optical absorption imaging [29,47]. We note that for our system, $t_{\rm meas}(\sim 24.6\,{\rm ms}) \ll \Gamma^{-1}(\sim 60\,{\rm s})$, which means the proposed measurement can be carried out practically in real time before the BEC rotation is damped significantly.

To characterize the extent to which the superfluid components are disturbed by the rotation measurement, we have also calculated the fidelity $F(t) = \int_{-\pi}^{\pi}[\psi_\sigma^*(\phi,t)\psi_\sigma(\phi,0)]^2 d\phi$ of the wave functions over time, as shown in Fig. 3(e). As can be seen, the fidelity stays around 0.9 over 4 s. From detailed analyses, we have found that the decrease in fidelity is more due to the transition from the uniform density condensate to the solitonic state (as part of the OAM transfer mechanism) and less due to the rotation measurement (i.e., interaction with the light field). This confirms the minimally destructive nature of our measurement technique.

We now analyze the variation of the peak locations and separations on relevant experimental parameters, as shown in Fig. 4. This allows us to account for experimental parameter variations and to optimize configurations where possible. In the figure, the solid lines are from the Bogoliubov analysis, and the markers denote numerical simulation data. As can be seen in Fig. 4(a) the peak splitting ($|\omega_{2+} - \omega_{2-}|$) increases with current-current interaction between species $\mathcal{G}_d'$ (and becomes resolvable even in absence of lattice rotation), which can be modified by the choice of different initial Zeeman states via the scattering length $a_{s_{\sigma\sigma'}}$ [40]. The variation in the peak splitting of the peak on the topological charge ℓ of the LG beam is shown in Fig. 4(c). The location of the ω_{2+} peak is shown in Figs. 4(b) and 4(d) as a function of $\mathcal{G}_d'$ and ℓ, respectively. The variation of the peak splitting and ω_{2+} peak location with the lattice rotation (Ω') is shown in Figs. 4(e) and 4(f). In all cases, the simulations and the Bogoliubov analysis agree well. These results provide a template for mapping experimental data and determining the AB drag factor of the two interacting superfluids. Before concluding, we emphasize that while all figures in this paper relate to the physics of the system, only the cavity transmission spectra (and ensuing sensitivity, splittings, etc.) can be measured with minimal destruction. The condensate density and phase profile measurements, for example, would result in the complete destruction of the condensates and have only been provided to clarify the physics.

IV. CONCLUSION

We have theoretically introduced a detection paradigm for observing the heretofore undetected AB effect, which predicts dissipationless drag to be exerted by one superfluid upon another. In contrast to other AB detection methods in existence, our proposal allows for real-time, *in situ*, minimally destructive, resolution-amplified and three orders-of-magnitude more sensitive measurement of the AB effect using experimentally available spinor BECs in ring traps and standard optical cavities and beams. Our theoretical analysis is based on numerical simulations of the stochastic quantum hydrodynamic equations as well as analytic Bogoliubov theory, which show good agreement with each other. In our proposal, we have presented condensate density and phase profiles, matter-wave orbital angular momentum spectra, cavity output spectra, and measurement sensitivities and fidelities. Our proposal brings the powerful techniques of cavity optomechanics, which enabled the detection of gravitational waves, to the study of rotationally interacting superfluids. We expect our work to have fundamental implications for ongoing studies of superfluid hydrodynamics, atomtronics, matter-wave interferometry, cosmological simulations, and cavity optomechanical sensing.

ACKNOWLEDGMENTS

M.B. thanks the Air Force Office of Scientific Research (FA9550-23-1-0259) for support. R.K. acknowledges support from JSPS KAKENHI Grant No. JP21K03421. We also gratefully acknowledge our supercomputing facility Param-Ishan (IITG), where all the simulation runs were performed.

APPENDIX A: QUENCH-INDUCED SUPERCURRENTS IN SPINOR BEC

In this section, we show an example of the generation of supercurrents in spinor BEC through chemical potential quenching, which simulates the cooling of the BEC [36]. In the spinor BEC, quenching the chemical potential leads to phase winding in one or both components depending on how the quench affects internal states. To simulate this phenomenon, we numerically solve the nondimensionalized two-component stochastic quantum hydrodynamic equation, which takes the form

$$\begin{aligned}(i-\Gamma)\frac{d\psi_\sigma}{d\tau} = &-\frac{d^2\psi_\sigma}{d\phi^2} + \frac{U_0}{\omega_\beta}|\alpha|^2\cos^2(\ell\phi)\,\psi_\sigma \\ &- \Omega'\left(-i\frac{d}{d\phi}\right)\psi_\sigma - \mu_\sigma\,\psi_\sigma + (\mathcal{G}_{\sigma\sigma}|\psi_\sigma|^2 \\ &+ \mathcal{G}_{\sigma\sigma'}|\psi_{\sigma'}|^2)\,\psi_\sigma + \mathcal{G}_{d_\sigma}\,(\mathcal{J}'_{\sigma\sigma} + \mathcal{J}'_{\sigma\sigma'}) \\ &+ \xi(\phi,\tau).\end{aligned} \tag{A1}$$

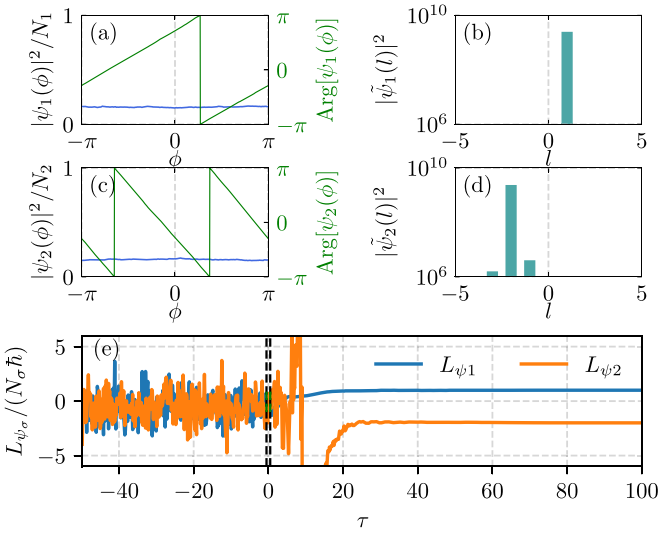

FIG. 5. [(a) and (c)] Condensate density (blue) and phase (green) profiles and [(b) and (d)] corresponding matter-wave OAM distributions of the quench-induced supper-currents ψ_1 and ψ_2 obtained at the end of the simulation, indicating $L_{p1} = 1$ and $L_{p2} = -2$. (e) Temporal evolution of angular momentum of the two components. The black dashed lines indicate the quench period ($\tau = -5$ to 5). Here $\tau_{\text{quench}} = 0.1$, $\Omega' = -1$, $\mathcal{G}' = 0.8$, $\mathcal{G}'_d = 0.095$, $\mathcal{G}_{d_\sigma} = \mathcal{G}'_d/\rho_\sigma$, $\rho_\sigma = N_\sigma/2\pi$, $\Gamma = 0.01$, and $T = 10$ nK.

Here $(\sigma, \sigma') \in 1, 2, \sigma \neq \sigma'$, and ψ_σ refers to the condensate wave function of component σ. The quench on the chemical potential follows the following protocol given by [36]:

$$\mu(\tau) = \begin{cases} -\mu_0 & \text{for } \tau < -\tau_{\text{quench}}, \\ \mu_0 \frac{\tau}{\tau_{\text{quench}}} & \text{for } \tau \in [-\tau_{\text{quench}}, \tau_{\text{quench}}], \\ \mu_0 & \text{for } \tau > \tau_{\text{quench}}. \end{cases} \tag{A2}$$

Here $\tau_{\text{quench}} = 5$ and $\mu_0 = 50$. This protocol varies the chemical potential in the range $-\mu_0$ to μ_0 linearly in the time interval $-\tau_{\text{quench}} \leqslant \tau \leqslant \tau_{\text{quench}}$.

The condensate density profile, phase profile, and OAM distributions for the two superflow cases are shown in Fig. 5. In Figs. 5(a) and 5(c), the density profiles are scaled by the norm of each component. From the phase profiles and the OAM distribution, it is clear that the ψ_1 state has obtained the winding number $L_{p_1} = 1$, whereas for the other component, the winding number $L_{p_2} = -2$. The quench dynamics of the angular momentum of both components throughout $-50 < \tau < 150$ are shown in Fig. 5(e). This allows the system to stabilize thermally and one of the components to acquire a nonzero winding number. Here it should be noted that, due to the stochastic nature of the system, the winding number of the induced superflows is different for different realizations. Thus we have similarly realized $L_{p1} = 3$, $L_{p2} = 0$ as used in the main text.

APPENDIX B: BOGOLIUBOV–DE GENNES ANALYSIS

In this section, we present the Bogoliubov–de Gennes (BdG) analysis for our model. The quantum hydrodynamic equation, including the current-dependent atomic interactions, takes the form [25,29,31]

$$\begin{aligned} i\hbar\frac{d\psi_\sigma}{dt} = &-\frac{\hbar^2}{2mR^2}\left[\frac{d^2}{d\phi^2} + \Omega'\left(-i\frac{d}{d\phi}\right)\right]\psi_\sigma \\ &+ \hbar U_0|\alpha|^2\cos^2(\ell\phi)\psi_\sigma + (g_{\sigma\sigma}|\psi_\sigma|^2 \\ &+ g_{\sigma\sigma'}|\psi_{\sigma'}|^2)\psi_\sigma + g_{d_{\sigma\sigma}} m\,\mathcal{J}_{\sigma\sigma} + g_{d_{\sigma\sigma'}} m\,\mathcal{J}_{\sigma\sigma'}, \end{aligned} \tag{B1}$$

where $\sigma, \sigma' \in (1, 2)$, $\sigma' \neq \sigma$. In this equation, along with the rotational kinetic energy, potential energy due to the optical lattice, and the conventional density-dependent atomic interactions, we have the last two terms on the right-hand side that represent the current-dependent atomic interactions, having the form

$$\begin{aligned} \mathcal{J}_{\sigma\chi} = &\left[2(\partial_\phi\psi_\sigma)(\psi^*_\chi\partial_\phi\psi_\chi - \psi_\chi\partial_\phi\psi^*_\chi)\right. \\ &\left. + \psi_\sigma(\psi^*_\chi\partial^2_\phi\psi_\chi - \psi_\chi\partial^2_\phi\psi^*_\chi)\right](\hbar/2mRi)^2, \end{aligned} \tag{B2}$$

where $\chi \in (\sigma, \sigma')$. To obtain the excitation spectrum, we perturb the spatially uniform state, replacing it with $\psi_\sigma = (\Phi_\sigma + \delta\Phi_\sigma)\,e^{-i\mu_\sigma t/\hbar}$. We obtain the linearized equations for the small perturbation $\delta\Phi_\sigma$ and using

$$\Phi_\sigma = \sqrt{\frac{N}{2\pi}}e^{iL_{p_\sigma}\phi} \tag{B3}$$

and

$$\delta\Phi_\sigma = e^{iL_{p_\sigma}\phi}\left[\frac{u_\sigma}{\sqrt{2\pi}}e^{i(\pm2\ell\phi-\omega t)} + \frac{v^*_\sigma}{\sqrt{2\pi}}e^{-i(\pm2\ell\phi-\omega^* t)}\right], \tag{B4}$$

we get

$$\begin{aligned} \hbar\omega[u_1 \quad v_1 \quad u_2 \quad v_2]^T &= M[u_1 \quad v_1 \quad u_2 \quad v_2]^T \\ &= (M_0 + M_{\text{int}} + g'_d\,M_{g_d}) \\ &\quad \times [u_1 \quad v_1 \quad u_2 \quad v_2]^T. \end{aligned} \tag{B5}$$

The matrix M_0, which includes the contributions from the rotational kinetic energy and the chemical potential is expressed as

$$M_0 = \begin{bmatrix} \hbar\omega_{1\pm} - \mu_1 & 0 & 0 & 0 \\ 0 & -\hbar\omega_{1\pm} + \mu_1 & 0 & 0 \\ 0 & 0 & \hbar\omega_{2\pm} - \mu_2 & 0 \\ 0 & 0 & 0 & -\hbar\omega_{2\pm} + \mu_2 \end{bmatrix}, \tag{B6}$$

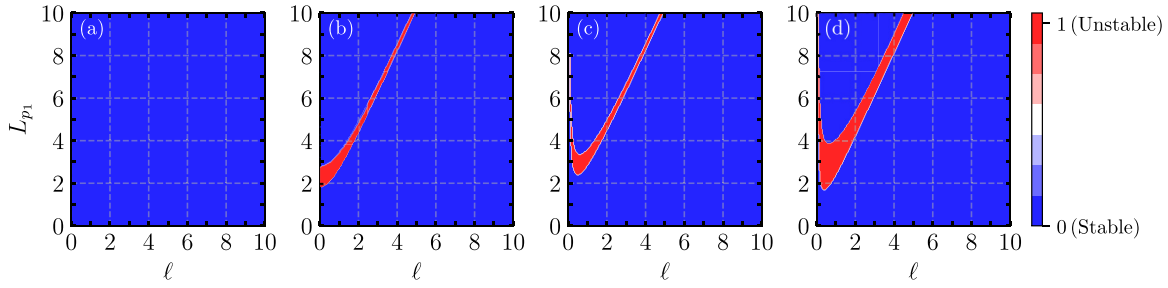

FIG. 6. Stability phase diagram for (a) $\mathcal{G}'_d = 0$ ($\mathcal{G}' = 0$), $\Omega' = 0$, (b) $\mathcal{G}'_d = 0.018$ ($\mathcal{G}' = 0.4$), $\Omega' = 0$, (c) $\mathcal{G}'_d = 0.018$ ($\mathcal{G}' = 0.4$), $\Omega' = -1$, and (d) $\mathcal{G}'_d = 0.095$ ($\mathcal{G}' = 0.8$), $\Omega' = -1$. In all the plots, $L_{p_2} = 0$ and $N = 1500$. The blue (red) region indicates the dynamically stable (unstable) region.

where $\omega_\beta = \hbar/(2mR^2)$, $\omega_{1\pm} = \hbar(L_{p_1} \pm 2\ell - \Omega'/2)^2/2I$, $\omega_{2\pm} = \hbar(L_{p_2} \pm 2\ell - \Omega'/2)^2/2I$, and

$$\mu_\sigma = \hbar\big[\omega_\beta\big(L_{p_\sigma}^2 - \Omega' L_{p_\sigma}\big) + 2N(\tilde{g}_{\sigma\sigma} + \tilde{g}_{\sigma\sigma'})\big] + \sum_{\chi=\sigma,\sigma'} g_{d_{\sigma\chi}} m\,(\hbar/2mRi)\,(\hbar/2mRi)\big[2\big(iL_{p_\sigma}\big)\big(2iL_{p_\chi}(N/2\pi)\big)\big]. \tag{B7}$$

The matrix M_{int} in Eq. (B5) represents the density-dependent atomic interaction energy and it is expressed as

$$M_{\text{int}} = 2N\hbar \begin{bmatrix} 2\tilde{g}_{11} + \tilde{g}_{12} & \tilde{g}_{11} & \tilde{g}_{12} & \tilde{g}_{12} \\ -\tilde{g}_{11} & -(2\tilde{g}_{11} + \tilde{g}_{12}) & -\tilde{g}_{12} & -\tilde{g}_{12} \\ \tilde{g}_{21} & \tilde{g}_{21} & 2\tilde{g}_{21} + \tilde{g}_{21} & \tilde{g}_{21} \\ -\tilde{g}_{21} & -\tilde{g}_{21} & -\tilde{g}_{21} & -(2\tilde{g}_{21} + \tilde{g}_{21}) \end{bmatrix}, \tag{B8}$$

where $\tilde{g}_{\sigma\chi} = g_{\sigma\chi}/(4\pi\hbar)$. The last term in Eq. (B5) represents the current-current coupling and it is expressed as

$$M_{g_d} = \begin{bmatrix} M_{11} & 4\big(-L_{p_1} + \ell\big)\big(L_{p_1} + \ell\big) & -4\big(L_{p_1} + \ell\big)\big(L_{p_2} + \ell\big) & 4\big(L_{p_1} + \ell\big)\big(-L_{p_2} + \ell\big) \\ -4\big(-L_{p_1} + \ell\big)\big(L_{p_1} + \ell\big) & M_{22} & -4\big(-L_{p_1} + \ell\big)\big(L_{p_2} + \ell\big) & 4\big(-L_{p_1} + \ell\big)\big(-L_{p_2} + \ell\big) \\ -4\big(L_{p_2} + \ell\big)\big(L_{p_1} + \ell\big) & 4\big(L_{p_2} + \ell\big)\big(-L_{p_1} + \ell\big) & M_{33} & 4\big(-L_{p_2} + \ell\big)\big(L_{p_2} + \ell\big) \\ -4\big(-L_{p_2} + \ell\big)\big(L_{p_1} + \ell\big) & 4\big(-L_{p_2} + \ell\big)\big(-L_{p_1} + \ell\big) & -4\big(-L_{p_2} + \ell\big)\big(L_{p_2} + \ell\big) & M_{44} \end{bmatrix}/(2i)^2. \tag{B9}$$

$$\begin{aligned} M_{11} &= -4\big(2L_{p_1}^2 + L_{p_1}L_{p_2} + 4L_{p_1}\ell + 2L_{p_2}\ell + \ell^2\big) \\ M_{22} &= 4\big(2L_{p_1}^2 + L_{p_1}L_{p_2} - 4L_{p_1}\ell - 2L_{p_2}\ell + \ell^2\big) \\ M_{33} &= -4\big(L_{p_1}L_{p_2} + 2L_{p_1}\ell + 2L_{p_2}^2 + 4L_{p_2}\ell + \ell^2\big) \\ M_{44} &= 4\big(L_{p_1}L_{p_2} - 2L_{p_1}\ell + 2L_{p_2}^2 - 4L_{p_2}\ell + \ell^2\big). \end{aligned} \tag{B10}$$

Here $g'_d = \hbar\omega_\beta \mathcal{G}'_d$ and $\mathcal{G}'_d = 2g_{d_{\sigma\chi}}(N/2\pi)$ is the drag factor. The eigenvalues of the above matrix M [Eq. (B5)] represent the sidemode frequencies of the BEC matter waves. Although in principle they can be obtained analytically, the expressions are cumbersome, and in practice we have calculated them numerically. The corresponding sidemode frequencies have been represented by dashed lines in the plots showing the power spectrum of the phase quadrature of the cavity output field in the main article.

APPENDIX C: COUNTERSUPERFLOW INSTABILITY

Countersuperflow instability occurs when the relative velocity between two superfluids is large enough to lead to the transfer of momentum aimed at reducing their relative momentum while conserving the total momentum in the system [45]. The system stability phase diagram for various values of interspecies atomic interactions is shown in Fig. 6, by considering the eigenfrequencies of matrix M [Eq. (B5)] as functions of the parameters L_{p1} and ℓ. In the absence of interactions, ($\mathcal{G}'_d = 0$) it can be seen from Fig. 6(a) that the system is dynamically stable for all values of L_{p_1}, ℓ within the ranges considered. In the presence of interactions ($\mathcal{G}'_d \neq 0$), the frequencies are complex inside the red region of Fig. 6(b), which indicates that the condensate is dynamically unstable for those values of L_{p_1} and ℓ. In this case, for a given ℓ, the condensates become dynamically unstable above a critical value of L_{p_1}. Rotation of the optical lattice results in the appearance of one more unstable branch, as shown in Fig. 6(c). For higher values of interspecies interactions, the critical value of L_{p_1} decreases,

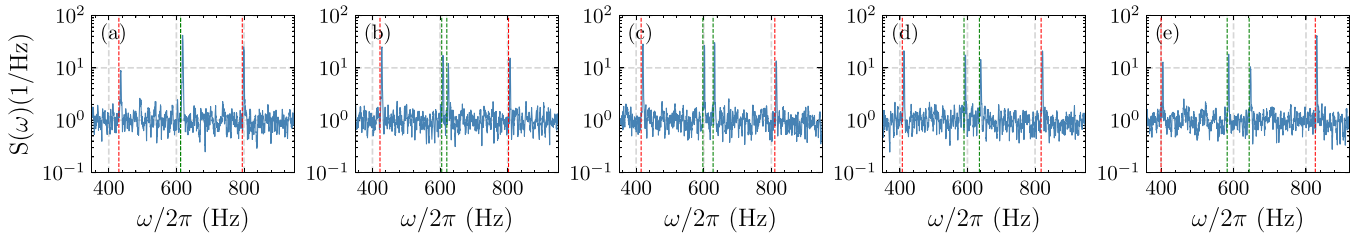

FIG. 7. Power spectra of the output phase quadrature of the cavity field for (a) $\Omega' = 0$, (b) $\Omega' = -0.25$, (c) $\Omega' = -0.5$, (d) $\Omega' = -0.75$, and (e) $\Omega' = -1$. The other parameters used are L_{ψ_2} for $L_{p_1} = 3$, $L_{p_2} = 0$, $N = 1500$, $\mathcal{G}' = 0.8$, $\mathcal{G}'_d = 0.095$, and $P_{\rm in} = 0.4\,$pW. Here the red (green) dashed lines denote the analytical predictions for the frequencies corresponding to $L_{p_1} \pm 2\ell - \Omega'/2$ ($L_{p_2} \pm 2\ell - \Omega'/2$) sidemodes, obtained from the BdG analysis.

and the width of the unstable region increases. These findings are similar to the earlier analysis for only density-dependent atomic interactions [46].

APPENDIX D: DYNAMIC BRAGG SPECTROSCOPY: LATTICE ROTATION

In this section we demonstrate the dynamic Bragg spectroscopy method used by us to amplify the peak splitting in the cavity spectrum. Essentially, by rotating the weak optical lattice at angular frequency, Ω' the separation between the first order Bragg diffraction peaks can be varied [30].

This effect can be seen in Fig. 7, which shows cavity spectra for various values of Ω'. There is no rotation ($\Omega' = 0$) in Fig. 7(a), where the peak splitting $\omega_{2+} - \omega_{-}$ is not resolvable for our parameters. In contrast, Figs. 7(b) and 7(e) show how the peak splitting becomes clearly and increasingly resolvable for increasing values of Ω'.

APPENDIX E: CALCULATION OF THE DRAG FACTOR

In a two-component BEC having equal component densities $\rho_1 = \rho_2$ and the drag density ρ_d, the drag factor is related to the intraspecies and interspecies atomic interactions $g_{\sigma\sigma}$ and $g_{\sigma\sigma'}$, respectively, and is expressed analytically using Bogoliubov theory as [13]

$$\mathcal{G}'_d = 2\frac{\rho_d}{\rho_1} = \frac{16\eta^2}{3\pi}\frac{1}{(\sqrt{2(\gamma+\eta)}+\sqrt{2(\gamma-\eta)})^3}, \tag{E1}$$

where $\rho_d/\rho_1 = g_{d_{\sigma\chi}}\rho_1$. Here $\gamma = 2g_{\sigma\sigma}m/\hbar^2 n$ and $\eta = 2g_{\sigma\sigma'}m/\hbar^2 n$ are the dimensionless atomic interaction strengths, n is the total BEC density defined as $n = (2N)/(2\pi R)$, and $g_{\sigma\chi} = 2\hbar\omega_\rho a_{s_{\sigma\chi}}/R$ denotes the reduced atomic interactions. After substituting the values provided in the main article, we get $g_{\sigma\sigma} = 1.16 \times 10^{-35}$. Considering $g_{\sigma\sigma'} = \mathcal{G}' g_{\sigma\sigma}$, for $\mathcal{G}' = \{0.1, 0.2, 0.3, 0.4, 0.5, 0.6, 0.7, 0.8, 0.9\}$, we obtain $\mathcal{G}'_d = \{0.001, 0.004, 0.01, 0.018, 0.029, 0.045, 0.066, 0.095, 0.141\}$.

APPENDIX F: POWER SPECTRUM OF ANGULAR MOMENTUM OF THE TWO COMPONENTS

In this section, we have calculated the Fourier transform of the time series of the angular momentum per atom of both superfluid components, which yields the characteristic frequencies of the angular momentum variation and compared it with the cavity output spectrum. The power spectrum of the phase quadrature of the cavity output field for $L_{p_1} = 3$, $L_{p_2} = 0$, and $\mathcal{G}'_d = 0.095$ ($\mathcal{G}' = 0.8$) is shown in Fig. 8(a). As explained in the main article, we see four peaks, corresponding to the $L_{p_1} \pm 2\ell - \Omega'/2$ and $L_{p_2} \pm 2\ell - \Omega'/2$ sidemodes at the locations predicted by the Bogoliubov analysis.

The Fourier transformations of the angular momenta per atom L_{ψ_1} are shown in Fig. 8(b). In this plot, the dominant peaks correspond to $L_{p1} \pm 2\ell - \Omega'/2$ due to the initial motion of the ψ_1 component. In addition, peaks corresponding to the winding number of the other component, namely ψ_2, also

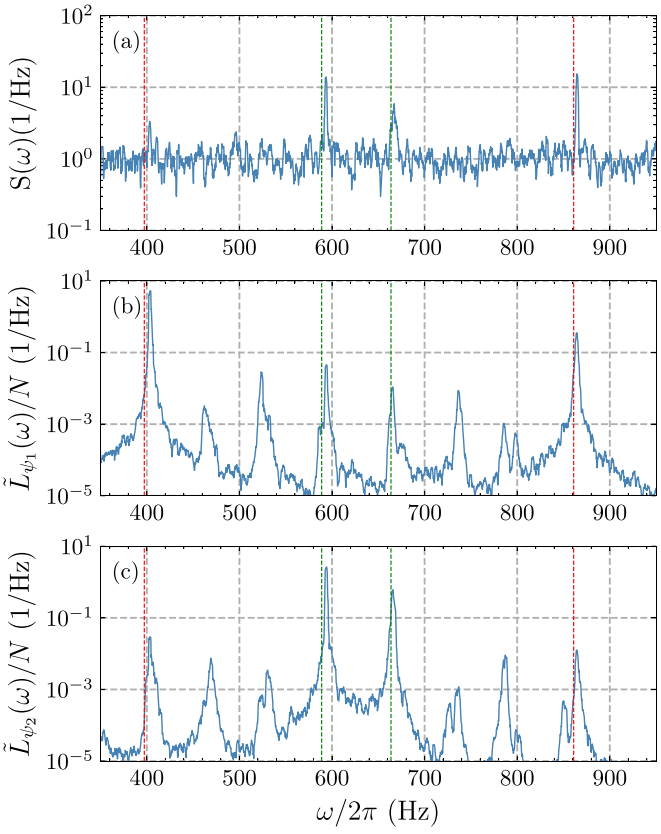

FIG. 8. (a) The power spectrum of the phase quadrature of the cavity output field, (b) the power spectrum of L_{ψ_1}, and (c) the power spectrum of L_{ψ_2} for $L_{p_1} = 3$, $L_{p_2} = 0$, $\Omega' = -1$, $N = 1500$, $\mathcal{G}' = 0.8$, $\mathcal{G}'_d = 0.095$, and $P_{\rm in} = 0.4\,$pW. The red (green) dashed lines denote the analytical predictions for the frequencies corresponding to $L_{p_1} \pm 2\ell - \Omega'/2$ ($L_{p_2} \pm 2\ell - \Omega'/2$) side modes and were obtained from the Bogoliubov analysis.

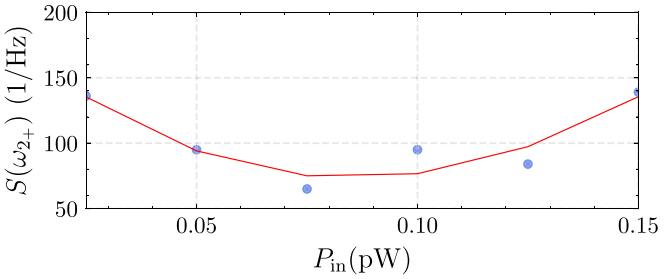

FIG. 9. Variation of the peak height at ω_{2+} with input optical power. The other parameters used are the same as in Fig. 8. The red line denotes a third-order polynomial curve that fits the data points.

appear, signifying the presence of angular momentum exchange. The contribution of the current-interaction-driven AB effect is larger than that of the countersuperflow instability, making the frequency splitting resolvable. The other (unlabeled) peaks in the spectrum appear due to the involvement of the neighboring modes of $L_{p_1} \pm 2\ell - \Omega'/2$ and $L_{p_2} \pm 2\ell - \Omega'/2$ in the dynamics of the transition from the uniform density state to the density modulated state. The Fourier transformation of the angular momentum per atom L_{ψ_2} is likewise shown in Fig. 8(c) and has a similar explanation.

APPENDIX G: EFFECT OF INPUT OPTICAL POWER ON THE CAVITY OUTPUT SPECTRA

The power spectrum of the phase quadrature of the cavity output field normalized to the steady-state photon number for various input optical power values is shown in Fig. 9.

Here we have focused on the ω_{2+} peak corresponding to the initially nonrotating condensate ($L_{p_2} \pm 2\ell - \Omega'/2$), which is the object being measured in our protocol. Increasing the input power initially improves signal to noise, decreasing the optical shot noise. After a certain value of input power ($P_{\rm in} = 0.075$ pW), the noise level begins to increase due to back action noise [29]. This figure indicates the existence of a standard quantum limit, and hence the optimum measurement power value of $P_{\rm in} = 0.075$ pW, where the optical shot noise and back action noise due to the radiation pressure force are balanced [29,35].

APPENDIX H: AB DRAG EFFECT IN A POPULATION-IMBALANCED BEC

In this section, we investigate a spinor BEC with unequal particle numbers ($N_1 \neq N_2$), a case that is more experimentally accessible than the balanced spinor. We show the condensate density, phase profiles, the corresponding matter-wave OAM distributions, the angular momentum dynamics, and the power spectra of the output phase quadrature of the cavity field in Fig. 10. Remarkably, regardless of the unequal particle numbers, our proposed method is able to determine the drag factor from the cavity output spectra, providing a robust approach to detect the AB drag effect in an experimentally realistic setup.

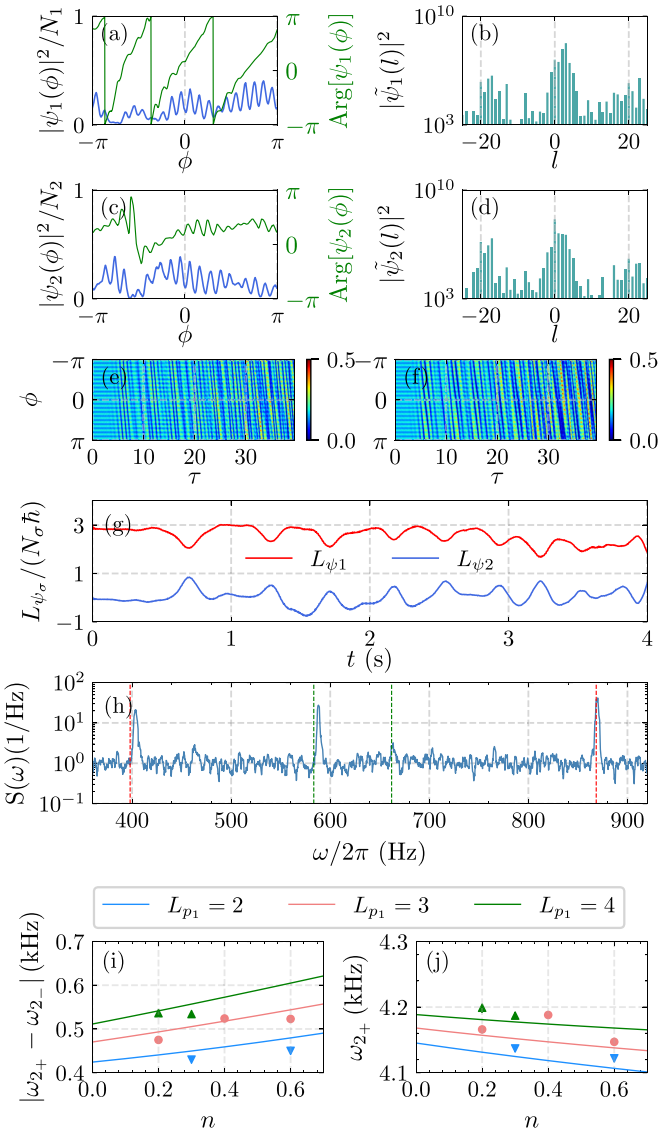

FIG. 10. [(a) and (c)] Condensate density (blue) and phase (green) profiles and [(b) and (d)] corresponding matter-wave OAM distributions of the two components ψ_1 and ψ_2 for $L_{p_1} = 3$, $L_{p_2} = 0$, $\ell = 10$, $N_1 = 1800$, $N_2 = 1200$, $\Omega' = -1$, $\mathcal{G}' = 0.8$, $\mathcal{G}'_d = 0.095$, and $P_{\rm in} = 0.4$ pW. [(e) and (f)] The pseudocolor representation of the condensate density profile evolution scaled by N_σ for ψ_1 and ψ_2, respectively. (g) Temporal evolution of the angular momenta per atom of the two components. (h) Power spectra of the output phase quadrature of the cavity field. Here the red (green) dashed lines denote the analytical predictions for the frequencies corresponding to $L_{p_1} \pm 2\ell - \Omega'/2$ ($L_{p_2} \pm 2\ell - \Omega'/2$) sidemodes, obtained from the BdG analysis. (i) Variation of the magnitude of the peak splitting $|\omega_{2+} - \omega_{2-}|$ and (j) Variation of the peak location of ω_{2+} with the population imbalance $n = \frac{N_1 - N_2}{N_1 + N_2}$.

[1] A. F. Andreev and E. P. Bashkin, Three-velocity hydrodynamics of superfluid solutions, Sov. J. Exp. Theor. Phys. **42**, 164 (1975).

[2] J.-M. Duan and S. Yip, Supercurrent drag via the Coulomb interaction, Phys. Rev. Lett. **70**, 3647 (1993).

[3] N. Chamel, Superfluidity and superconductivity in neutron stars, J. Astrophys. Astron. **38**, 43 (2017).

[4] A. F. Aminov, A. A. Sokolik, and Y. E. Lozovik, Superfluid drag between excitonic polaritons and superconducting electron gas, Quantum **6**, 787 (2022).

[5] C. J. Pethick and H. Smith, *Bose-Einstein Condensation in Dilute Gases* (Cambridge University Press, Cambridge, UK, 2008).

[6] J. Polo, W. J. Chetcuti, E. C. Domanti, P. Kitson, A. Osterloh, F. Perciavalle, V. P. Singh, and L. Amico, Perspective on new implementations of atomtronic circuits, Quantum Sci. Technol. **9**, 030501 (2024).

[7] D. V. Fil and S. I. Shevchenko, Nondissipative drag of superflow in a two-component Bose gas, Phys. Rev. A **72**, 013616 (2005).

[8] J. Nespolo, G. E. Astrakharchik, and A. Recati, Andreev–Bashkin effect in superfluid cold gases mixtures, New J. Phys. **19**, 125005 (2017).

[9] M. Ota and S. Giorgini, Thermodynamics of dilute Bose gases: Beyond mean-field theory for binary mixtures of Bose-Einstein condensates, Phys. Rev. A **102**, 063303 (2020).

[10] E. K. Dahl, E. Babaev, and A. Sudbø, Unusual states of vortex matter in mixtures of Bose-Einstein condensates on rotating optical lattices, Phys. Rev. Lett. **101**, 255301 (2008).

[11] V. Karle, N. Defenu, and T. Enss, Coupled superfluidity of binary Bose mixtures in two dimensions, Phys. Rev. A **99**, 063627 (2019).

[12] D. Romito, C. Lobo, and A. Recati, Linear response study of collisionless spin drag, Phys. Rev. Res. **3**, 023196 (2021).

[13] L. Parisi, G. E. Astrakharchik, and S. Giorgini, Spin dynamics and Andreev-Bashkin effect in mixtures of one-dimensional Bose gases, Phys. Rev. Lett. **121**, 025302 (2018).

[14] F. Carlini and S. Stringari, Spin drag and fast response in a quantum mixture of atomic gases, Phys. Rev. A **104**, 023301 (2021).

[15] D. Contessi, D. Romito, M. Rizzi, and A. Recati, Collisionless drag for a one-dimensional two-component Bose-Hubbard model, Phys. Rev. Res. **3**, L022017 (2021).

[16] Y. Sekino, H. Tajima, and S. Uchino, Spin conductivity spectrum and spin superfluidity in a binary Bose mixture, Phys. Rev. Res. **5**, 023058 (2023).

[17] J. Linder and A. Sudbø, Calculation of drag and superfluid velocity from the microscopic parameters and excitation energies of a two-component Bose-Einstein condensate in an optical lattice, Phys. Rev. A **79**, 063610 (2009).

[18] P. P. Hofer, C. Bruder, and V. M. Stojanović, Superfluid drag of two-species Bose-Einstein condensates in optical lattices, Phys. Rev. A **86**, 033627 (2012).

[19] K. Sellin and E. Babaev, Superfluid drag in the two-component Bose-Hubbard model, Phys. Rev. B **97**, 094517 (2018).

[20] A. Syrwid, E. Blomquist, and E. Babaev, Dissipationless vector drag—Superfluid spin Hall effect, Phys. Rev. Lett. **127**, 100403 (2021).

[21] E. Blomquist, A. Syrwid, and E. Babaev, Borromean supercounterfluidity, Phys. Rev. Lett. **127**, 255303 (2021).

[22] M. Pylak, F. Gampel, M. Płodzień, and M. Gajda, Manifestation of relative phase in dynamics of two interacting Bose-Bose droplets, Phys. Rev. Res. **4**, 013168 (2022).

[23] L. Amico, D. Anderson, M. Boshier, J.-P. Brantut, L.-C. Kwek, A. Minguzzi, and W. von Klitzing, *Colloquium*: Atomtronic circuits: From many-body physics to quantum technologies, Rev. Mod. Phys. **94**, 041001 (2022).

[24] J. Polo, W. J. Chetcuti, T. Haug, A. Minguzzi, K. Wright, and L. Amico, Persistentcurrents in ultracold gases, arXiv:2410.17318.

[25] A. Syrwid, E. Blomquist, and E. Babaev, Drag-induced dynamical formation of dark solitons in Bose mixture on a ring, Phys. Rev. Res. **4**, L042003 (2022).

[26] K. Hossain, S. Gupta, and Michael McNeil Forbes, Detecting entrainment in Fermi-Bose mixtures, Phys. Rev. A **105**, 063315 (2022).

[27] R. Cominotti, A. Berti, A. Farolfi, A. Zenesini, G. Lamporesi, I. Carusotto, A. Recati, and G. Ferrari, Observation of massless and massive collective excitations with Faraday patterns in a two-component superfluid, Phys. Rev. Lett. **128**, 210401 (2022).

[28] S. Beattie, S. Moulder, R. J. Fletcher, and Z. Hadzibabic, Persistent currents in spinor condensates, Phys. Rev. Lett. **110**, 025301 (2013).

[29] P. Kumar, T. Biswas, K. Feliz, R. Kanamoto, M.-S. Chang, A. K. Jha, and M. Bhattacharya, Cavity optomechanical sensing and manipulation of an atomic persistent current, Phys. Rev. Lett. **127**, 113601 (2021).

[30] N. Pradhan, P. Kumar, R. Kanamoto, T. N. Dey, M. Bhattacharya, and P. K. Mishra, Ring Bose-Einstein condensate in a cavity: Chirality detection and rotation sensing, Phys. Rev. A **109**, 023524 (2024).

[31] N. Pradhan, P. Kumar, R. Kanamoto, T. N. Dey, M. Bhattacharya, and P. K. Mishra, Cavity optomechanical detection of persistent currents and solitons in a bosonic ring condensate, Phys. Rev. Res. **6**, 013104 (2024).

[32] D. Naidoo, K. Aït-Ameur, M. Brunel, and A. Forbes, Intracavity generation of superpositions of Laguerre–Gaussian beams, Appl. Phys. B **106**, 683 (2012).

[33] F. Orsi, N. Sauerwein, R. P. Bhatt, J. Faltinath, E. Fedotova, N. Reiter, T. Cantat-Moltrecht, J.-P. Brantut, Cavity microscope for micrometer-scale control of atom-photon interactions, PRX Quantum **5**, 040333 (2024).

[34] T. Mithun, S. C. Ganguli, P. Raychaudhuri, and B. Dey, Signatures of two-step impurity-mediated vortex lattice melting in Bose-Einstein condensates, Europhys. Lett. **123**, 20004 (2018).

[35] M. Aspelmeyer, T. J. Kippenberg, and F. Marquardt, Cavity optomechanics, Rev. Mod. Phys. **86**, 1391 (2014).

[36] A. Das, J. Sabbatini, and W. H. Zurek, Winding up superfluid in a torus via Bose Einstein condensation, Sci. Rep. **2**, 352 (2012).

[37] D. Tan and Z. Chen, On a general formula of fourth order Runge-Kutta method, J. Math. Sci. Math. Educ. **7**, 1 (2012).

[38] K. C. Wright, R. B. Blakestad, C. J. Lobb, W. D. Phillips, and G. K. Campbell, Driving phase slips in a superfluid atom circuit with a rotating weak link, Phys. Rev. Lett. **110**, 025302 (2013).

[39] S. Eckel, J. Lee, F. Jendrzejewski, N. Murray, C. W. Clark, C. J. Lobb, W. D. Phillips, M. Edwards, and G. K. Campbell,

Hysteresis in a quantized superfluid 'atomtronic' circuit, Nature (London) **506**, 200 (2014).

[40] S. Knoop, T. Schuster, R. Scelle, A. Trautmann, J. Appmeier, M. K. Oberthaler, E. Tiesinga, and E. Tiemann, Feshbach spectroscopy and analysis of the interaction potentials of ultracold sodium, Phys. Rev. A **83**, 042704 (2011).

[41] C. N. Weiler, T. W. Neely, D. R. Scherer, A. S. Bradley, M. J. Davis, and B. P. Anderson, Spontaneous vortices in the formation of Bose–Einstein condensates, Nature (London) **455**, 948 (2008).

[42] M. Aidelsburger, J. L. Ville, R. Saint-Jalm, S. Nascimbène, J. Dalibard, and J. Beugnon, Relaxation dynamics in the merging of N independent condensates, Phys. Rev. Lett. **119**, 190403 (2017).

[43] Y. Guo, R. Dubessy, M. d. G. de Herve, A. Kumar, T. Badr, A. Perrin, L. Longchambon, and H. Perrin, Supersonic rotation of a superfluid: A long-lived dynamical ring, Phys. Rev. Lett. **124**, 025301 (2020).

[44] F. Brennecke, S. Ritter, T. Donner, and T. Esslinger, Cavity Optomechanics with a Bose-Einstein condensate, Science **322**, 235 (2008).

[45] H. Takeuchi, S. Ishino, and M. Tsubota, Binary quantum turbulence arising from countersuperflow instability in two-component Bose-Einstein condensates, Phys. Rev. Lett. **105**, 205301 (2010).

[46] C. K. Law, C. M. Chan, P. T. Leung, and M.-C. Chu, Critical velocity in a binary mixture of moving Bose condensates, Phys. Rev. A **63**, 063612 (2001).

[47] A. Kumar, N. Anderson, W. D. Phillips, S. Eckel, G. K. Campbell, and S. Stringari, Minimally destructive, Doppler measurement of a quantized flow in a ring-shaped Bose–Einstein condensate, New J. Phys. **18**, 025001 (2016).